

AD-A129 479

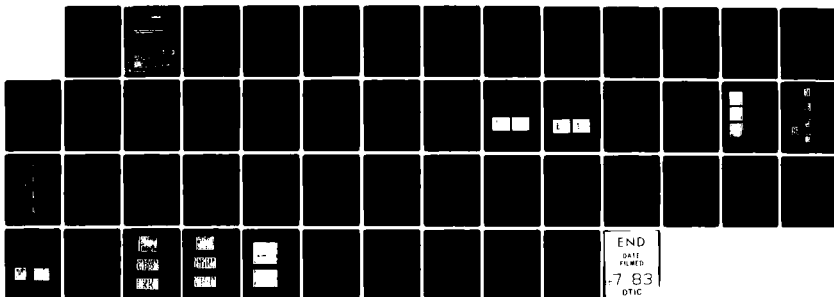
HIGH EXTRACTION FREE-ELECTRON LASER EXPERIMENTS(U)
MATHEMATICAL SCIENCES NORTHWEST INC BELLEVUE WA
29 MAR 83 MSNW-C.11.240 N00014-82-C-0704

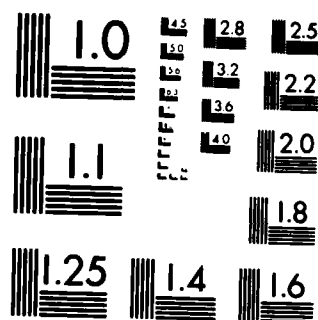
1/1

UNCLASSIFIED

F/G 20/5

NL





MICROCOPY RESOLUTION TEST CHART
NATIONAL BUREAU OF STANDARDS 1963-A

ADA 1 29479

Contract N00014-82-C-0704

NSNW C.11.240

HIGH EXTRACTION FREE-ELECTRON LASER EXPERIMENTS

Submitted to
Office of Naval Research
Arlington, Virginia 22217

By
Mathematical Sciences Northwest, Inc.
2755 Northup Way
Bellevue, Washington 98004

DTIC
ELECTE
JUN 20 1983
A

29 March 1983

This document has been approved
for public release and sale; its
distribution is unlimited.

SUMMARY

During this reporting period a tapered-wiggler free-electron laser experiment has been constructed and initial energy extraction measurements have been made. The intent of the experiment is to demonstrate the high extraction capability of the tapered-wiggler free-electron laser. The hardware involves three primary elements: a two meter Sm Co₅ permanent magnet wiggler, an RF linac operating at 20 MEV, and a 500 megawatt pulsed CO₂ laser. The FEL is operated in an amplifier configuration, with the electron and laser beams making a single simultaneous pass through the wiggler. The interaction of these beams is monitored by comparison of the electron energy spectrum with and without the presence of the CO₂ laser. The spectrum measurements are made using a round pole electron spectrometer. The wiggler wavelength is tapered such that the exit resonant energy is 9 percent below that at the entrance. The extraction measurements show that some electrons do decelerate 9 percent, in accordance with the taper, and that the net extraction is 2.5 percent. Extraction of 4 percent is expected when the overlap between electron and photon beams is improved.

Approved for			
Special Agent			
in Charge			
<i>Letter in file</i>			
Approved			
Special Agent			
in Charge			
Dist	Special		
<i>A</i>			

CONTENTS

Section	Page
SUMMARY	ii
1 INTRODUCTION	1-1
2 HARDWARE	2-1
2.1 Electron Beamline	2-1
2.2 Electron Spectrograph	2-3
2.3 Wiggler Magnet	2-4
2.4 CO ₂ Laser	2-12
3 TESTING AND EXPERIMENTAL DATA	3-1
3.1 Electron Beam Characterization	3-1
3.2 Extraction Measurements	3-6
4 SUBHARMONIC PREBUNCHING INJECTOR	4-1
4.1 SHPB Injector Design	4-1
4.2 SHPB Injector Performance Measurements	4-8
5 SUMMARY	5-1
REFERENCES	R-1

Section 1

INTRODUCTION

This document is the midterm report for the DARPA/Mathematical Sciences Northwest (MSNW) FEL Program covering the 18-month period ending September 30, 1982. The overall goal of the program during this period has been the characterization of the tapered-wiggler FEL. In particular, it is intended to demonstrate that the tapered wiggler can provide significant electron kinetic energy extraction on a single pass through the wiggler structure. It is expected that the tapered wiggler will lead to the development of high efficiency FEL's requiring only modestly efficient electron energy recovery.

The tapered-wiggler concept is a modification of the original FEL concept demonstrated at Stanford.⁽¹⁾ Tapering, or slowly changing the wiggler wavelength from the front to the rear of the wiggler, allows the resonant interaction to be maintained as electrons decelerate. Substantial deceleration requires quite large optical power, and the tapered wiggler will, therefore, tend to operate at lower optical gain than would an equivalent system with an untapered wiggler. For this reason, the experiment described here is done in a low gain amplifier configuration using an external high power conventional laser to generate the input beam. The development of Linac technology necessary to obtain high peak electron current for eventual oscillator operation with the tapered wiggler has also been addressed in this program.

The experiments are being done in cooperation with the Boeing Aerospace Corporation, who is providing the RF Linac and associated e-beam hardware and technology. A block diagram of the experiment is shown in Figure 1-1. The output of a gigawatt class CO₂ laser and the 20 MeV beam

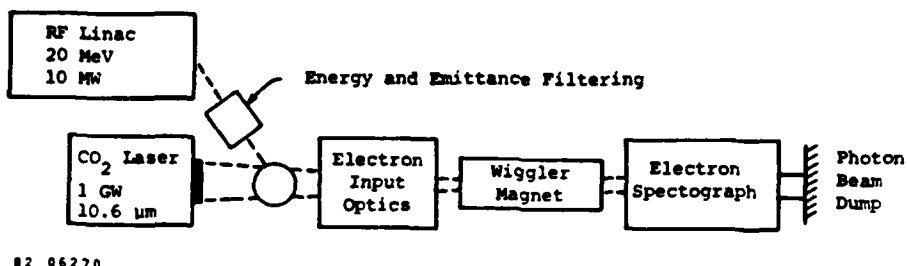


Figure 1-1. Block Diagram of Apparatus for Single-Pass Electron Energy Spectrum Measurement.

from the RF Linac make a single simultaneous pass through the wiggler magnet. After exiting the wiggler, the electrons are energy analyzed in a single-magnet spectrograph. This spectrograph is the primary diagnostic of the experiment, and is used to measure the shift in the electron centroid energy which results from the FEL interaction. The wiggler magnet is tapered such that the exit resonant energy is 9 percent lower than that at the entrance, and the expected shift of the centroid is about half this value. Ideally, about half of the electrons decelerate by 9 percent, while others are spread over a several percent width centered at the input energy. With a spectrograph resolution of 0.5 percent, the spectrum measurement is relatively simple and completely unambiguous.

The schematic diagram of the electron beamline is shown in Figure 1-2. The Boeing Linac is a 30 MeV traveling wave radio-frequency

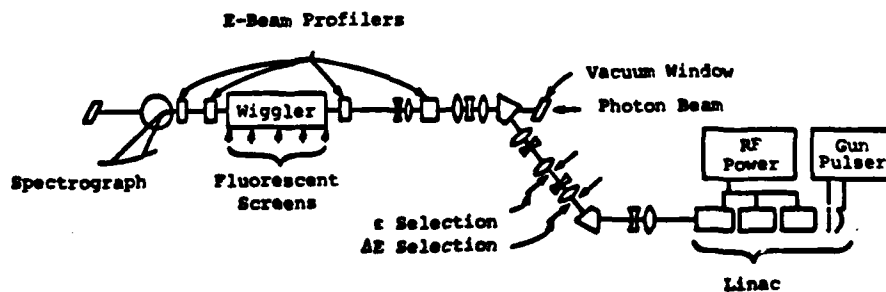


Figure 1-2. Schematic of Electron Beamline.

linear accelerator. The primary power is supplied by a single 20 megawatt peak, 20 kilowatt average, S-Band klystron. A grided gun provides macropulse width over the range 0.005-10 microseconds. Bunchers are used to compress the charge into 15-20 degrees of phase of the accelerating wave to achieve an energy spread of less than 2 percent. The output pulse train consists of 20 picosecond pulses separated by the 350 picosecond RF cycle time. The CO₂ laser pulse is 40 ns long, so that roughly 100 micropulses interact with CO₂ pulse. The portion of the macropulse interacting with the CO₂ laser is seen clearly in the time resolved electron energy spectrum, but the individual micropulse structure is not resolved. A feature of the electron translation system is that locations with energy and emittance encoding occur at convenient locations outside the magnet elements. Mechanical slits are used in these locations for selection of energy width and emittance. Wire scan profile monitors immediately upstream of the wiggler are used to set the input steering, beam size, and convergence. Five fluorescent targets within the wiggler magnet facilitate monitoring of the electron beam to ensure proper overlap with the CO₂ laser beam. The spectrograph designed for this program is a 12-inch round pole, Brown-Beuchner⁽²⁾ type. The energy range is 16 to 22 MeV. The focal plane is segmented into 20 channels with each channel cabled to an independent oscilloscope trace. The spectrograph detection bandwidth is greater than 200 megahertz. A fundamental limit to spectrograph resolution is the magnification due to beam size and beam divergence. This results in a resolution of $\Delta E/E = 0.002$, but the 20 discrete channels of the segmented focal plane reduce the actual resolution to 0.5 percent.

In accordance with the need for high current micropulses for eventual tapered-wiggler oscillator operation, Boeing has installed a subharmonically bunched injector on the accelerator as part of this program. The injector utilizes a standing wave RF cavity at the sixth subharmonic of the accelerating frequency to prebunch the gun output beam. The performance data presented in this report show 100-150 amps peak current and an emittance of 2-5 π mm mr at 20 MeV, with an energy

spread of less than 2 percent. This new injector was installed after some of the beam quality measurements recorded in the following sections were made, but it was used for all extraction measurements. This injector could be operated with or without subharmonic bunching, and all the extraction measurements were made without the buncher.

Section 2 contains a technical discussion of the electron beamline, spectrograph, CO₂ laser, and the wiggler magnet. The system testing and experimental results are found in Section 3. These results show that electrons can be decelerated 9 percent in accordance with a wiggler taper, and that net deceleration as large as 2.5 percent has been achieved. It is anticipated that 4 percent net extraction will be possible with improvement in the electron-photon overlap. Linac modification for operation with the subharmonic buncher is described in Section 4, and Section 5 is a summary.

Section 2

HARDWARE

2.1 ELECTRON BEAMLINE

The layout of the electron beam transport system for FEL experiments is illustrated schematically in Figure 2-1. Note that the description of

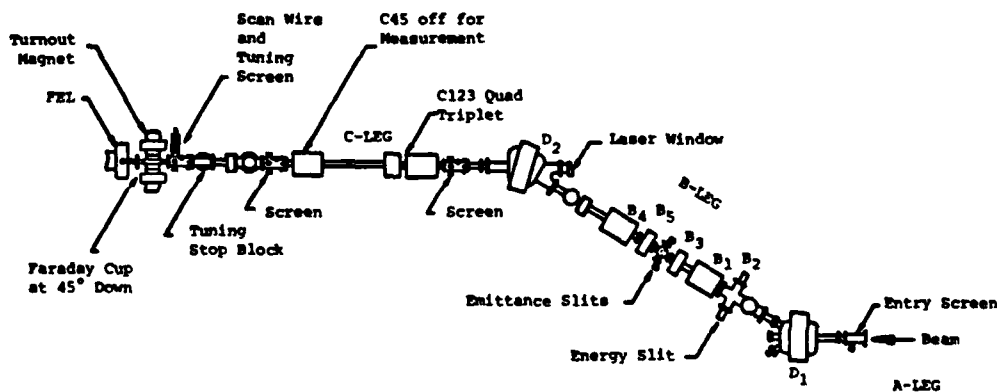


Figure 2.1. Schematic Layout of FEL Beamline.

the beamline is categorized into three sections, the A, B, and C legs. The first, labeled the A-leg, is approximately three meters long from the exit of the Linac to the first wedge bending magnet. This leg contains optical focusing control by means of a quadrupole doublet, which serves to control beam size input for the next section of the system. The start of this section, the B-leg, is the magnet D_1 which deflects the beam by 30° . At the focus of D_1 is a set of adjustable energy slits. Typically, the slits are set at 9 mm which limits the electron beam energy spread to 2 percent. There are six quadrupoles in the B-leg designated B_1 , B_2 , B_{3a} , B_{3b} , B_4 , and B_5 . These are placed symmetrically with respect to the center of the B-leg and operated in pairs (B_1 with B_5 , B_2 with B_4 , and B_{3a}

with B_{3D}). Their settings are such that the B-leg is achromatic with no focusing or magnification. In effect, the B-leg acts like a drift space and is similar to the system described by Swenson.⁽³⁾ A natural consequence of this arrangement is an energy focus at the center, i.e., beam sizes at the center are dominated by the natural emittance and not the energy spread. The third section, C-leg (approximately four meters) takes the beam from the exit of wedge D_2 to the entrance of the wiggler. The C-leg contains five quadrupoles C_1 and C_5 . An important function of these quadrupoles is to focus the electron beam in such a way that the optimum interaction in the photons is achieved. Specifically, this means a horizontal waist at the wiggler entrance and a vertical waist at the wiggler center. The operation of the B-leg is determined by the transfer characteristics of the dogleg. In contrast, the A- and C-legs are set depending on the phase space characteristics of the electron beam. In principle, this means the B-leg can be set once, while the A- and C-leg settings reflect the changes in beam emittance encoding from the Linac.

The design of the beamline was accomplished with the first order magnetic optics programmed in the TRANSPORT code.⁽²⁾ The basic matrix formulation is given by K.L. Brown, et al. The actual code was prepared by a collaboration among workers at SLAC (Palo Alto, California), NAL (Batavia, Illinois), and CERN (Geneva, Switzerland). The code simulates a beamline containing a variety of elements selected from a built-in menu (e.g., drift spaces, bend magnets, quadrupoles, solenoids, etc.). The simulation can be carried out explicitly to second order. A valuable feature of the code is its ability to vary certain user prescribed features automatically to fit desired beamline characteristics (e.g., focusing, achromaticity, phase space constraints, etc.).

A companion code, TURTLE,⁽⁴⁾ can trace rays through the same transport system described by the TRANSPORT code. This code also can simulate second order effects. The output from TURTLE is via histograms. These can be one-dimensional histograms of any of the six-phase space variables, horizontal and vertical positions, trajectory angles, energy

spread, and pulse length, or they can be two-dimensional to correlate any two of the phase space variables.

2.2 ELECTRON SPECTROGRAPH

The principal diagnostic for the high extraction FEL experiment was a 20-channel electron spectrometer. This device was designed to accept the relatively low divergence output beams from the wiggler. The spectrometer resolution is limited to about 0.2 percent due to effects of beam size, divergence, and steering errors. The actual resolution is determined by the segmented detection plane, which was divided into 0.5 percent and 1 percent kinetic energy slices. For most of the testing, adjacent channels were wired together resulting in ten data channels. The data channels were recorded on ten oscilloscopes with >200 MHz measurement bandwidth.

The details of the spectrograph design are driven by the requirements of the free electron laser experiments. Overall energy extraction from the electron beam can be measured by the difference between the electron spectra before and after the photon/electron interaction. The nominal electron beam input energy corresponds to $\gamma_{in} = 37.9$ ($T_0 = 18.86$ MeV). Theoretical predictions indicate that the greatest energy shift will correspond to $\gamma_{sum} = 34.4$ (about 9 percent). Allowances are made on both ends of this scale so that the spectrograph range is from 16.36 MeV to 19.63 MeV. The input electron spectrum was typically 2 percent wide and centered within 2 percent of the nominal input channel at 18.86 MeV. Since the input spectrum is rather narrow, energy bands around T_0 each of width $0.005 T_0$ were used. To measure the spectrum modified by the photon/electron interaction, 12 bands of $0.01 T_0$ width (10 below and 2 above the previous 8) provided the necessary range. The foregoing information is illustrated in Figure 2-2.

2.3 WIGGLER MAGNET

The permanent magnet wiggler has SmCo_5 bars arranged as shown in Figure 2-3. This scheme, first suggested by Halbach,⁽⁵⁾ makes efficient

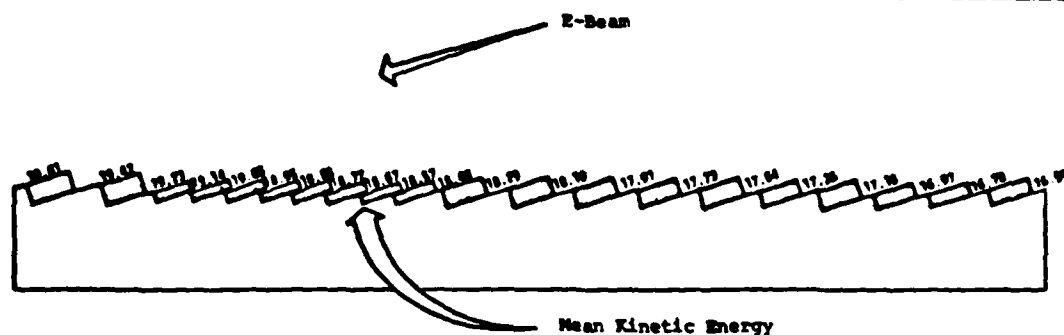


Figure 2-2. Ten Percent Extraction Spectrographic Array Design and Photo.

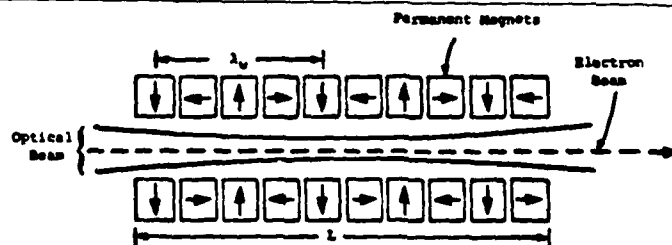


Figure 2-3. Planar Wiggler Geometry. Bold arrows on the SmCo_5 permanent magnets indicate the direction of magnetization. The wiggler actually has $96 \frac{3}{4}$ wavelengths, λ_w , within the total length, L .

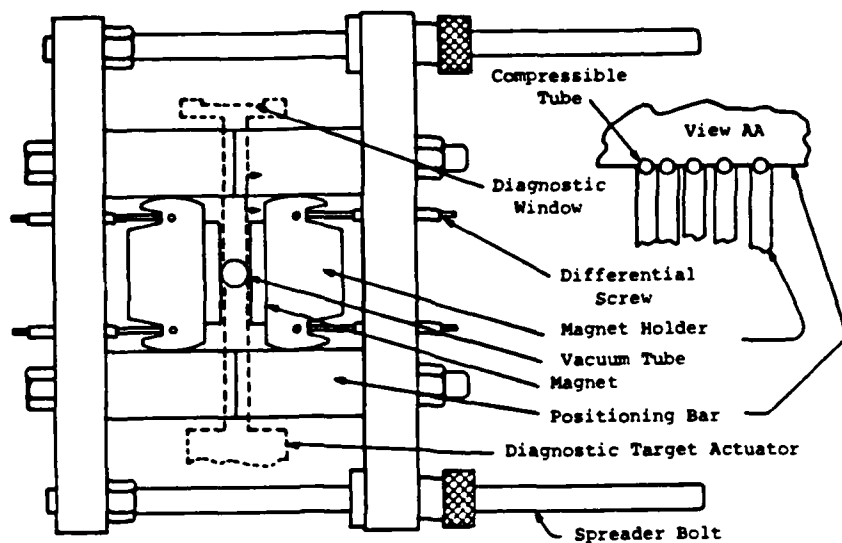
use of the magnetic material and produces a plane polarized field. Parameters, such as the gap and magnetic field wavelength, are optimized⁽⁶⁾ to minimize the photon power required to achieve a given deceleration. The photon beam is focused in the center of the wiggler with a design Rayleigh range of 65 cm, and is clipped at the entrance and exit at e^{-8} of the centerline intensity. This results in an on-axis intensity modulation of about ± 4 percent.⁽⁷⁾ Basic parameters of the wiggler are given in Table 2-1. Slow variation of the resonant energy along the wiggler length is achieved by change of wavelength at constant gap, with the resonant energy decreasing by 9 percent from entrance to exit. The tapering is chosen so that the stable phase angle is independent of axial position. For this taper, the calculated onset of trapping begins at approximately 100 MW photon power.

Aspects of the mechanical design are depicted in the end-view diagram in Figure 2-4. Each magnet is cemented to a separate aluminum holder

Table 2-1

WIGGLER PARAMETERS

Total Length	231 cm
Full Gap (magnetic)	1.27 cm
Peak Entrance Field	2.64 kG
Peak Exit Field	2.44 kG
Entrance Wavelength	2.54 cm
Exit Wavelength	2.22 cm
Remanent Field	8800 G
Magnet Dimensions	0.56 X 0.83 X 5.0 cm ³



82 06272

Figure 2-4. End View Diagram of Clamshell Wiggler Sections Enclosing the Vacuum Tube. Dotted lines indicate the three fluorescent screen diagnostic ports within the wiggler.

which is, in turn, positioned axially by slots in the positioning bars. The wiggler taper is determined by the location of these slots and can be changed by replacement of the positioning bars. Differential screws provide adjustment of the distance between the center line and each magnet for field tuning purposes and, in addition, allow magnet rotation in the plane of the figure. Such canting is useful for control of e-beam focal properties. For example, with increasing cant angle, the focal strength in the horizontal plane (as drawn) becomes weaker, while the vertical plane begins to focus.

A 1/2-inch O.D., 0.010-inch wall, Type 310 stainless steel vacuum tube is located between the two halves of the magnet assembly. The tube has five diagnostic ports, one each at the front and rear of the wiggler, and three along its length. Fluorescent screens can be inserted remotely at each port for determination of photon and electron beam positions and profiles. In practice, the beam from a helium-neon laser is made to run along the same line as the CO₂ laser, and the e-beam is positioned on the helium-neon laser spots.

The SmCo_5 magnets have nonuniformities which can lead to a reduction of the FEL interaction. The dominant nonuniformities important in this experiment are the average level of magnetization and the orientation of the magnetization vector with respect to the magnet body. The resulting departure of the wiggler field from the ideal value causes two separate problems. First, some trapped particles are lost from the ponderomotive potential well because of phase and amplitude noise in the B-field. This field deviation occurs on a short length scale compared to the distance the electron travels while making one orbit in the potential well, so the noise tends to have only a small effect on the trapping. The second problem, much more important to this experiment, is electron beam steering caused by field errors. This steering can cause loss of beam overlap, but even if overlap is not lost a trapping loss can still result if electrons move to off-axis regions of higher B-field. In the higher field region, the resonant energy differs from that on-axis, and this difference can exceed the depth of the potential well.

Before assembly, a Hall probe was used to measure the B-field of individual magnets. The probe was placed at locations corresponding to the wiggler centerline, and significant variations from magnet to magnet in field strength and uniformity were found. The typical magnitude of field errors is given in Table 2-2. Figure 2-5 shows the definition of

Table 2-2
TYPICAL FIELD ERRORS OF INDIVIDUAL MAGNETS

Parameter	Steering		Typical Error
	Type A	Type B	
Strength	0.1 $\frac{\text{mrad}}{\text{1 percent}}$	0	± 2.0 percent
θ_{short}	≈ 0	0.2 $\frac{\text{mrad}}{\text{degrees}}$	± 2.0 degrees
θ_{long}	0.1 $\frac{\text{mrad}}{\text{degrees}}$	0.2 $\frac{\text{mrad}}{\text{degrees}}$	± 0.3 degrees

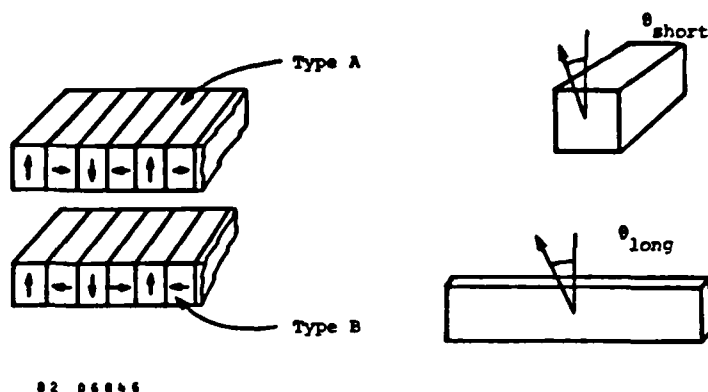


Figure 2-5. Definition of Symbols for Table 2-2.

type A and B magnets and the two angular errors θ_{short} and θ_{long} . The strength parameter is the field magnitude measured at the point of closest approach by the electron. If deviations occur randomly from magnet to magnet, they will result in trajectory errors which exceed the size of the photon beam. Accordingly, the magnets are arranged in the wiggler in such a manner as to compensate one another for field deviations. The magnet sorting algorithm developed has primary emphasis on reduction of steering errors while maintaining midplane symmetry, with phase and amplitude noise of the ponderomotive potential compensated to a lesser degree.

The field errors of the completed wiggler were measured and found to exceed the errors expected on the basis of simple summing of individual magnet fields. The magnitude of the phase and amplitude noise was 1 percent RMS in peak amplitude, and 1 percent RMS in wavelength, both of which are several times larger than expected. While the ponderomotive potential noise remained unimportant, the steering errors were significant and required correction.

This discrepancy between the sum of the individual fields and the actual field of the assembled wiggler may be due to demagnetization at the time of wiggler assembly. The demagnetizing H field for type A and type B magnets (as defined in Figure 2-5), when in the presence of the entire magnet array, is shown in Figure 2-6. These contours of H are calculated

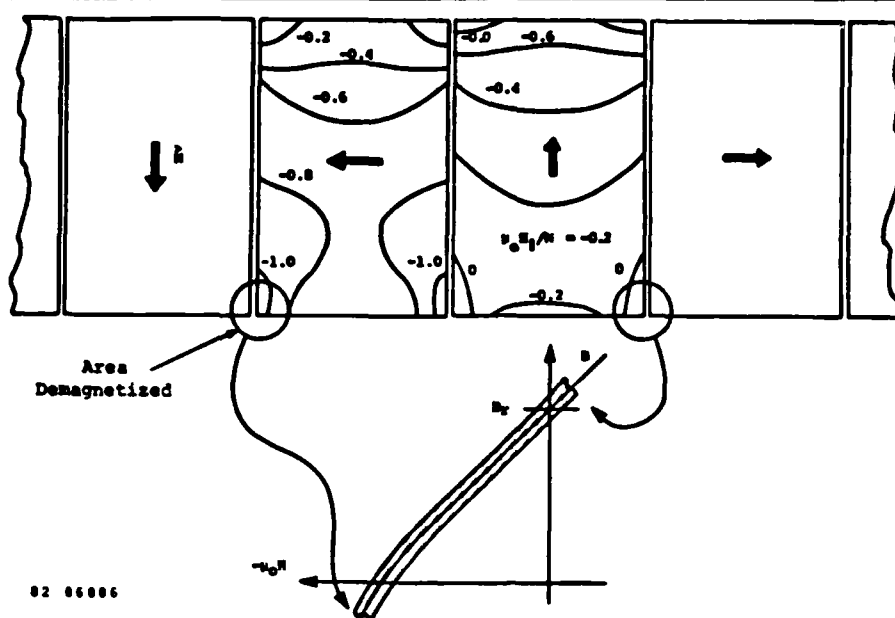


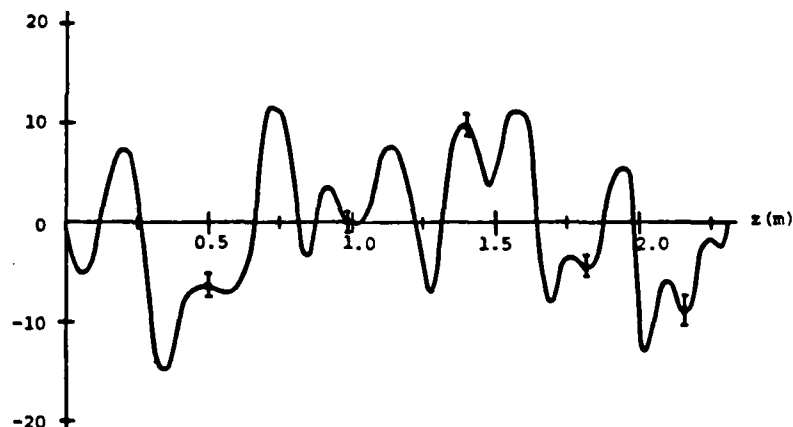
Figure 2-6. Demagnetizing Field for Magnets in Assembled Wiggler, the Contour Lines are of $\mu_0 H/M$, where $M (-B_r)$ is the Level of Magnetization. Only the H-field component in the direction of M is considered. The areas of $\mu_0 H/M \approx -1$ will suffer some demagnetization as shown by the gentle roll off in the B-H curve as $\mu_0 H/M$ approaches -1.

under the assumption of unity permeability (cgs units) and constant magnetization. The areas of $\mu_0 H/M \approx -1$ will suffer some permanent demagnetization. This loss of magnetization is the reason for the slight rolloff in the B-H curve as $\mu_0 H/M$ nears -1. Field errors will result if individual magnets demagnetize to differing degrees. Estimates indicate that demagnetization could easily account for the observed fields, but no definitive measurements were made which would indicate to what extent demagnetization affects this wiggler.

Fields of the completed wiggler have been measured with Hall probe and floating wire⁽⁸⁾ techniques. Probe orientation and linearity are both quite critical to obtaining reliable Hall probe data. As an independent check of the Hall probe data, the floating wire technique has been used in both transverse planes. In the wiggler plane, a several milliradian

steering error was found near the wiggler entrance. External Helmholtz trim coils were used for correction. Floating wire measurements with the trim coils in place indicate a maximum electron deviation of 0.2 mm in this plane.

In the plane of the B-field, a combination of floating wire and Hall probe techniques were used to assess steering. Application of the floating wire in this plane presents difficulty, because the wire tends to avoid the centerline due to B-field gradients. Obtaining quantitative steering measurements in this plane required analysis of the wire behavior, including the effect of the gradient.⁽⁹⁾ An example of the Hall probe measurement of the error field perpendicular to the B-field plane (nominally field free) is given in Figure 2-7. In this figure, a small



02 05917

Figure 2-7. Measured Error Field of Assembled Wiggler with Hall Probe Oriented to Measure Field Perpendicular to Nominal B-field Plane. The wiggler entrance is at $z = 0$ and exit is at $z = 2.3$ m. The data has been smoothed by averaging over several wiggler wavelengths.

oscillating component of the main wiggler field has been removed by averaging the data over several wiggler wavelengths. The oscillating component was of comparable magnitude to the error field. The error field shown could result from misalignment of magnetization vectors with respect to the magnet bodies (θ_{long} in Figure 2-5), or from slight misplacement of individual magnet bars within the wiggler.

The steering from these error fields acts synergistically with the focusing that results from the normal B-field transverse gradients. A calculated trajectory including steering errors and focusing is shown in Figure 2-8. It is calculated on the assumption that the electron enters the wiggler along the centerline, and shows that the calculated trajectory exceeds the $1/e$ point in the photon beam at two locations. The calculated trajectory, with correction coils in place, is also shown. The expected trajectory deviation in this plane is less than 0.3 mm. In practice, the e-beam is maintained on the wiggler centerline by adjustment of the correction coils while viewing the beam spots on the fluorescent screens within the wiggler.

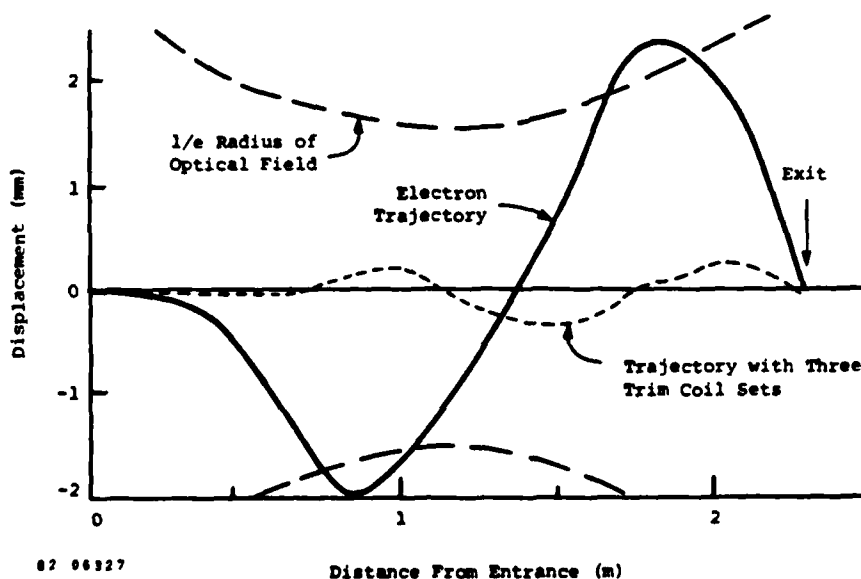
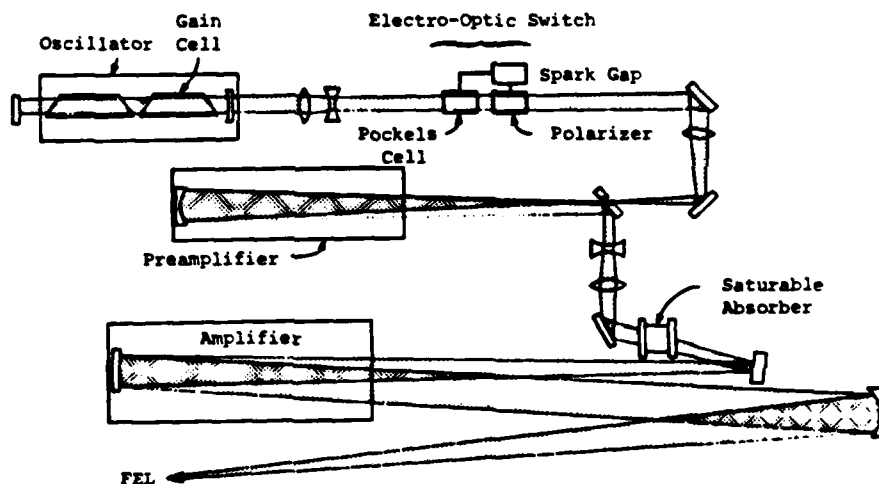


Figure 2-8. Calculated Trajectories in Nominal B-field Plane. The calculation is based on the field measurements of Figure 2-5 and the calculated focal properties in this plane.

2.4 CO₂ LASER

CO₂ laser is an oscillator-preamp-amplifier configuration built from Lumonics TEA units. A schematic diagram is shown in Figure 2-9. The Model 921 oscillator has a 50 cm gain length plus an additional 10 cm gain cell. The gain cell is a low pressure axial discharge which provides gain over a doppler line width which is narrow compared to the cavity mode spacing. When the gain cell is operating and the cavity is at a length which leaves some mode approximately overlapping the line of the gain cell, the system operates on a single longitudinal mode on the P-11 line of the 10 micron band. Single transverse mode operation is achieved with a single aperture near the rear mirror.

The oscillator output pulse is approximately 100 ns long, and this pulse is shortened before entering the preamp to 40 ns full width using an electro-optic switch. Without this pulse shortening the fluence on the NaCl vacuum interface window of the e-beam system would be unacceptably



82 06274

Figure 2-9. Block Diagram of the CO₂ Laser System.

large. Following the electro-optic switch, the beam makes a double pass through both the preamplifier and the amplifier, attaining approximately 10 J total energy. A saturable absorber cell is located between the preamplifier and amplifier in order to prevent self-oscillation. Typical pulse shapes after the amplifier are shown in Figures 2-10(a) and 2-10(b). Single mode operation is shown in (a) and multi-mode in (b). In both cases the measurements are made with a pyroelectric detector having a 500 picosecond risetime and a Tektronix 7844 scope. The detector views a portion of the radiation reflected from the NaCl vacuum window. The beat frequency in Figure 2-10(b) corresponds to the spacing of adjacent modes in the oscillator cavity. Single-mode operation is desirable from the standpoint of understanding the FEL interaction, and as seen in the figure appropriate single mode operation can be easily identified. Small length adjustments of the oscillator cavity are used to maintain the single mode condition.

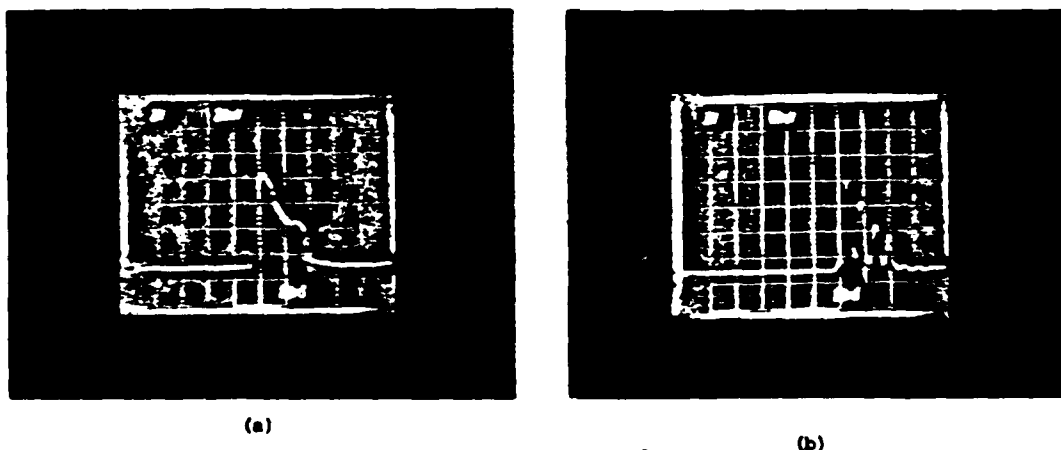


Figure 2-10. Time History of Amplifier Output. Trace (a) shows pulse shape with single longitudinal mode operation, and Trace (b) shows mode beating with multimode operation.

It is also desirable that the output beam be nearly diffraction-limited so that maximum possible intensity-length product can be achieved in the wiggler. Considerable care has been taken in the system design to avoid degradation of the beam. All optical elements with the exception of the mode control aperture in the oscillator are oversized at least to a diameter of 8ω , where ω is the calculated e^{-1} radius of the E-field based on calculated propagation of the initial TEM-00 wave exiting the oscillator cavity. Intensity profiles have been measured in the vicinity of the wiggler in order to get some feel for the beam quality as well as quantitatively confirm the desired Rayleigh range of about 65 cm. Profiles in both dimensions have been made with a linear pyroelectric detector array with 32 elements on 1 mm centers. A sample profile in a horizontal plane is shown in Figures 2-11(a) and 2-11(b). Traces (a) and (b) are taken at locations 3.2 meters and 2.4 meters upstream of the focus at the wiggler center, respectively. The change of profile with distance indicates that the system is not entirely defraction-limited in the sense that the beam can be described as a TEM-00 wave with some appropriate Rayleigh range, but no Strehl ratio measurements have been made. The focal spot at the center of the wiggler was too small to make useful profile measurements with this array.

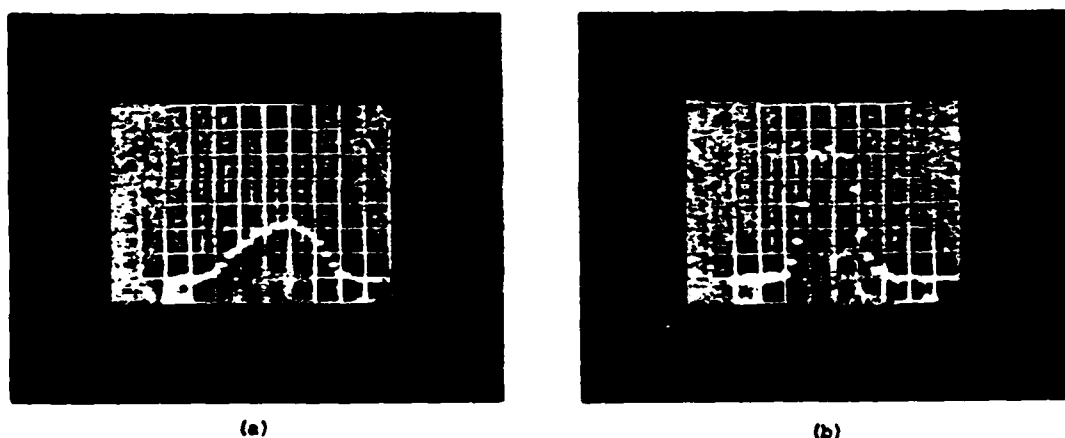


Figure 2-11. Horizontal Intensity Profile Upstream of the Wiggler. Profiles are made with a 32 element pyroelectric array, and are time integrated for one shot. Figures (a) and (b) are taken 3.2 and 2.4 meters upstream of the focus (at wiggler center), respectively.

Section 3

TESTING AND EXPERIMENTAL DATA

3.1 ELECTRON BEAM CHARACTERIZATION

The beam profile of the Linac was measured using six in-situ rotating wire beam profile scanners. Two scan boxes were located at the Linac output and were used in conjunction with Quads A1, A2 to measure accelerator output emittance and transport input conditions. Four more scanners were used in the FEL transport leg. These were symmetrically placed at the entrance and exit of the wiggler.

The profile monitor used a 0.5 mm tungsten alloy wire bent into a section of a 45° ellipse. As the wire rotates in the beam pipe, it cuts orthogonal axes after each 180° of rotation. The scan motor was rotated 45° to the pipe to provide both vertical and horizontal scanning.

Beam profiles were generated by observing the amplitude of the remaining (unscattered) beam at a downstream Faraday cup. (The technique requires an analysis magnet between the scanner and cup to insure rejection of small-angle scattered electrons.)

Oscilloscope display of Faraday cup current was gated to allow profiling of the beamshape in a specific time window. This was helpful in the current FEL experiment to profile that portion of the macropulse which the CO₂ laser pulse would overlap.

Horizontal and vertical axial centerlines were established by the FEL HeNe alignment laser. A detector diode pulse marked the signal loss as the wire cut the alignment beam. The time interval between the axis markers established the distance calibration at πr (r = the scan wire loop radius).

The wire scan detectors were used to measure the beam emittance before the wiggler was installed. For the measurement, a scanner was placed at the axial location that corresponded to the center of the wiggler. These data are shown in Figure 3-1. The traces were measured at full-width and full-width half-maximum. The percentage of charge involved in the emittance measurement is roughly 60 to 70 percent for the FWHM measurement, and 80 to 90 percent for the full-width measurement. Emittance is defined as follows:

$$\epsilon = \pi r_0 r_1 / L$$

r_0 = minimum radius at waist

r_1 = radius far from waist $r_1 \gg r_0$

L = distance from r_1 measurement to waist

for the data, the emittance values are:

	Vertical	Horizontal
60 to 70 percent charge	$\epsilon = 0.67 \text{ mm-mr}$	$\epsilon = 0.87 \text{ mm-mr}$
80 to 90 percent charge	$\epsilon = 1.47 \text{ mm-mr}$	$\epsilon = 5.07 \text{ mm-mr}$

In the horizontal plane, emittance values were probably at an upper limit since r_1 was not much greater than r_0 .

Beam scan data for the experiment with the wiggler in place are shown in Figures 3-2 and 3-3. The first data set were taken with the "old" electron gun in place (as in the measurement described above), and the second set after the installation of the high current injector. In comparing data, the beam from the new injector was roughly the same size as previous beams; however, stability of the beam was degraded. This was evidenced by the poor signal to noise ratio in the scan measurement, which relies on a reproducible Faraday cup trace as the display baseline. This instability prevented accurate emittance measurements, and made tuning the beam by using the scanners impractical. (In October 1982 this instability

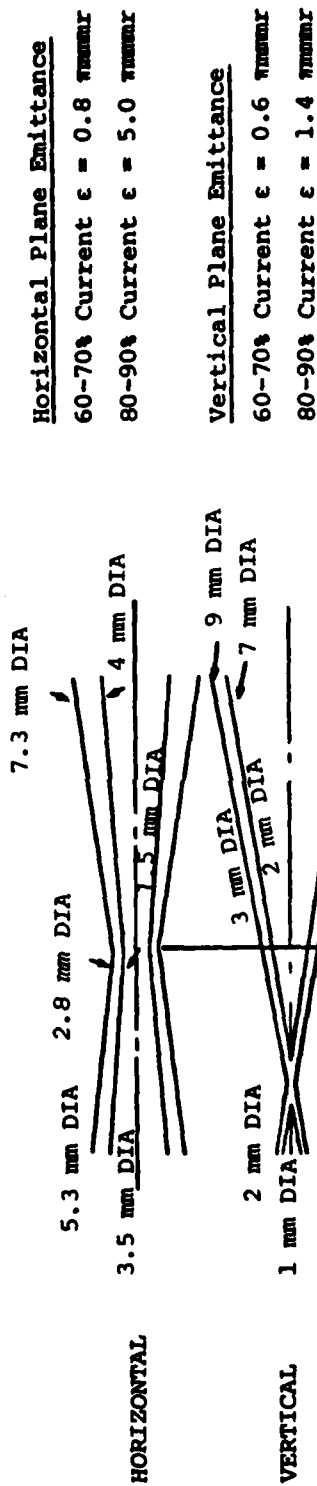
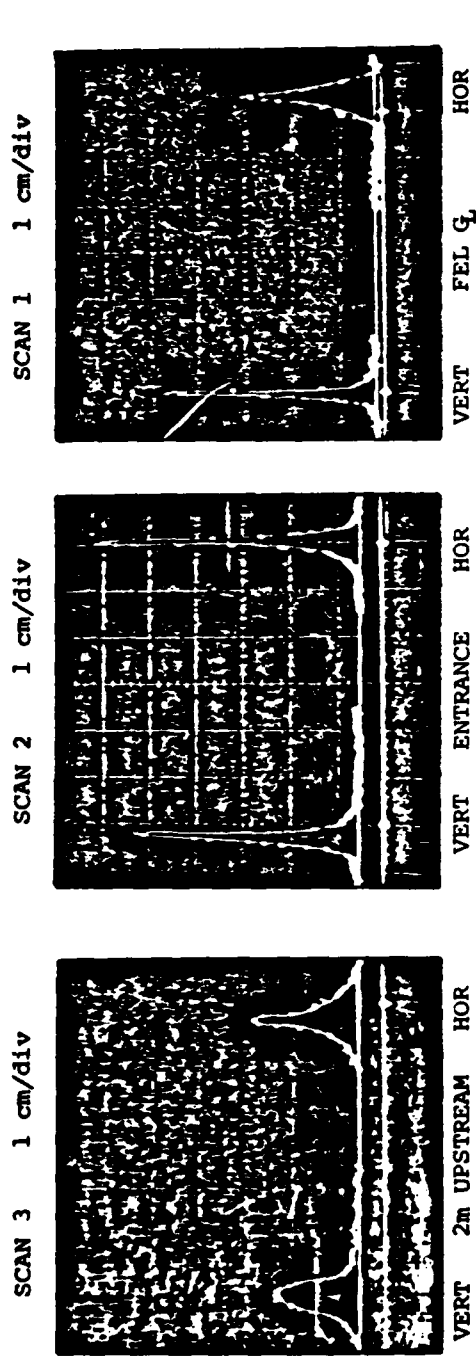
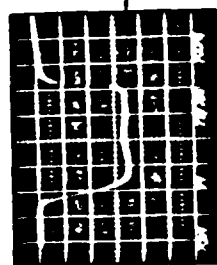


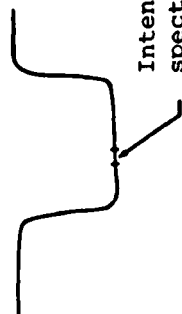
Figure 3-1. Emittance Profile at the Center of the FEL Wiggler.

ELECTRON BEAM PROFILE DATA

Current at
Spectrograph

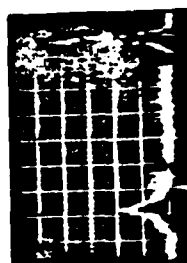


140mAmp



Intensified area of current at spectrograph identifies the portion of E-beam pulse used in profile data

SCAN
2.3 m from FEL entrance



low high left right

Beam Diameter 4.0mm 2.5mm FWHM

SCAN
.3 from FEL entrance

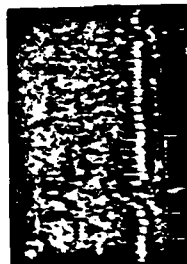


low high left right

3.0mm 2.5mm

Lower trace displays wire blank out of helium neon alignment laser

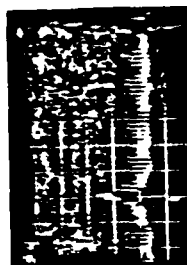
SCAN
.32m from FEL exit



low high left right

2.0mm 2.0mm

SCAN
2m from FEL exit



low high left right

4.0mm 2.5mm

Vertical Steering at FEL exit Omr

Vertical Steering at FEL Entrance 1.6mr Down

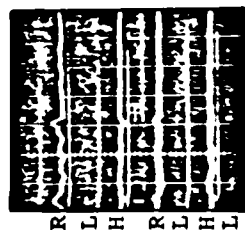
Figure 3-2. FEL Phase I Scan Monitor Data (Low Current Injector).

ELECTRON BEAM POSITION AND PROFILE DATA

9/16/81 240p

POSITION 1

50 cm from FEL entrance



POSITION 2

50 cm from FEL exit

Scan 1

2.3 from FEL entrance



Low High Left Right

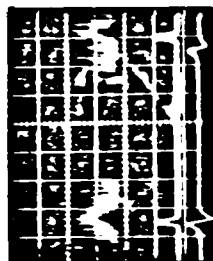
1.5 mm 1.5 mm

Q_L Q_L

FWHM Radius
Position with
Respect to Q_L

Scan 2

.3 m from FEL entrance



Low High Left Right

1.5 mm 2 mm

1 mm High 2 mm Right

Scan 3

.3 from FEL exit



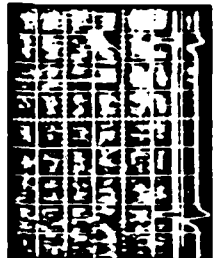
Low High Left Right

1.5 mm 1 mm

1 mm Low 1 mm Right

Scan 4

.8 m from FEL exit



Low High Left Right

1.5 mm 2 mm

1.8 mm Low Q_L

Fiducial Markers Generated by the Scanners

Wire Blank Out of Helium Neon Alignment Laser

Figure 3-3. FEL Phase I Scan Monitor Data (High Current Injector).

was traced to faulty circuitry in the RF drive. This circuit was repaired and beam stability was achieved for the December 1982 - January 1983 experiments.)

Fluorescent screens were added to the wiggler at five locations in January 1982 to assist in beam characterization. The screens, in combination with new dipole coils along the wiggler, were extremely useful in positioning the beam on axis through the experiment. However, quantitative data on beam size (and emittance) were not made using the screens due to three problems:

1. The light output from the phosphor was non-linear with current density.
2. The response of the TV system was not linear.
3. The phosphor was radiation sensitive and displayed both temporary and permanent damage mechanisms affecting output level.

3.2 EXTRACTION MEASUREMENTS

Electron energy gain or loss resulting from FEL interaction was measured with the electron spectrograph. In the experiments, interaction was identified in the time-resolved spectra, since the optical pulse is much shorter than the electron macropulse. While the temporal resolution is sufficient to resolve the FEL interaction on the macropulse, the individual micropulses are unresolved. The spectrograph array was cabled to ten oscilloscope channels in the connection sequence shown in Figure 3-4. Representative current histories are shown in Figure 3-5. In all

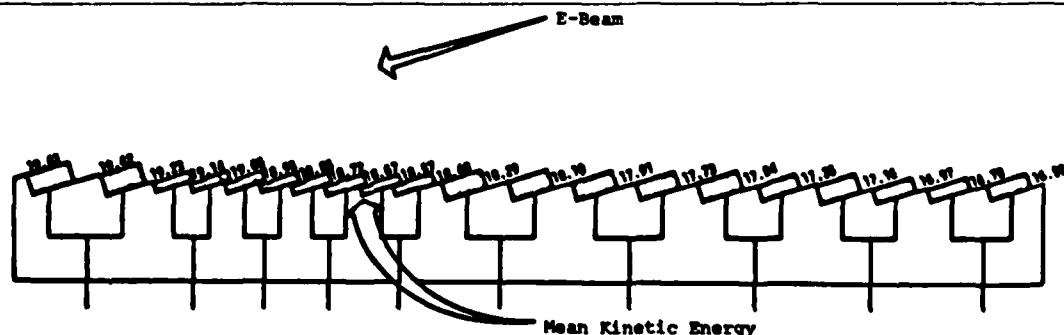
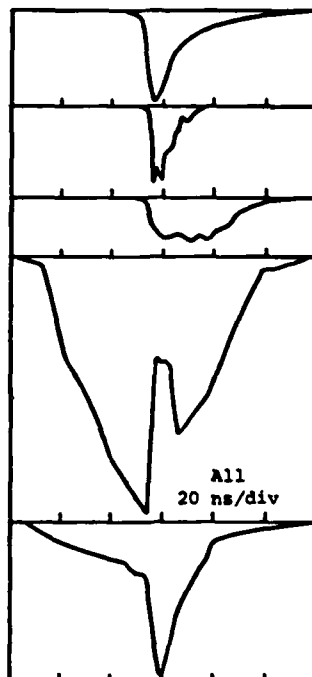


Figure 3-4. Spectrograph Detector Connecting Sequence for Phase I Extraction Data.

Shot 1146 2/16
2.5% Net Extraction



Laser 10J = 1 GW PK

9% Extraction
Near Linear Response

2% Extraction
Saturated Response

Nominal Energy
Large Current Loss

All
20 ns/div

High Nominal
Current Added

Figure 3-5. Time Resolved Photon/Electron Interaction Data.

cases, the abscissa represents time at 20 nanoseconds/division. The ordinates represent electron current, except Trace 1 which is laser power. The input electron beam appears mostly in Trace 4, which covers a 1 percent energy width at the nominal energy. (A small fraction of additional input current appears in Trace 5, which covers +1 to +2 percent from nominal). Trace 4 clearly shows a spike due to interaction with the optical pulses (Trace 1). The interaction momentarily reduces the current in this channel by about one-half. The current is displaced to both the energy gain and loss channels. Trace 2, which includes -8 to -10 percent energies, and Trace 3, which includes -2 to -4 percent, show only current resulting from the interaction.

The current pulse shape seen on any spectrograph channel is not expected to closely match the optical pulse because of nonlinear effects associated with the tapered-wiggler FEL. Trace 2, the resonant extraction

channel, shows a stronger relationship to photon power than Trace 3. This small energy loss channel shows a saturated value in the number of partially trapped electrons over a large range of photon power. Figure 3-6 is a comparison of the response of the resonant energy channel and the 2 percent loss channel plotted against input CO₂ laser power. (These data were taken from a single shot by time correlation of the response in the laser and two extraction channels.)

Electron energy spectra with and without the CO₂ laser beams are shown in Figure 3-7. The solid line shows the spectrum measured several

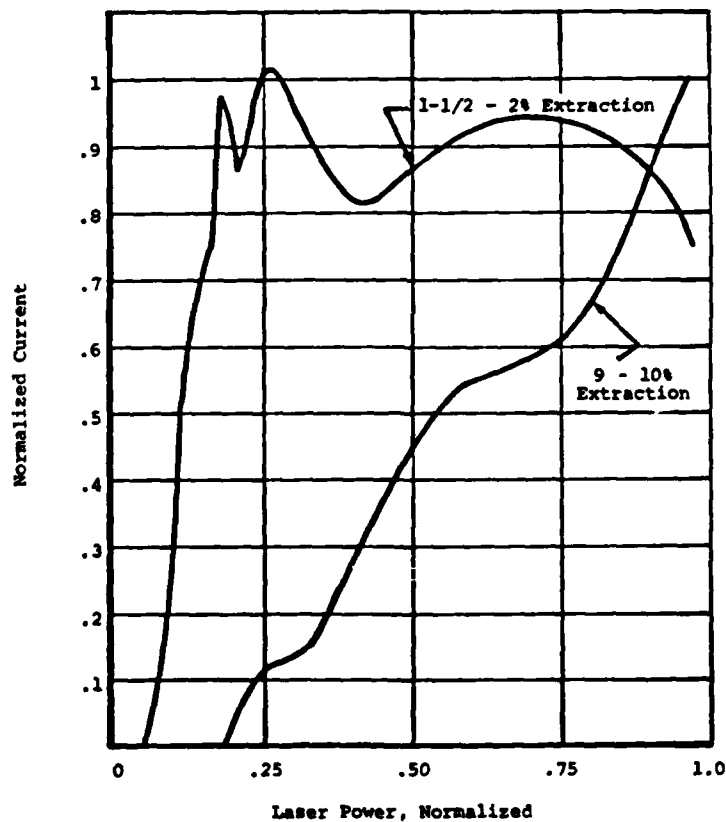


Figure 3-6. Resonant and 2 Percent Extraction as a Function of Laser Power.

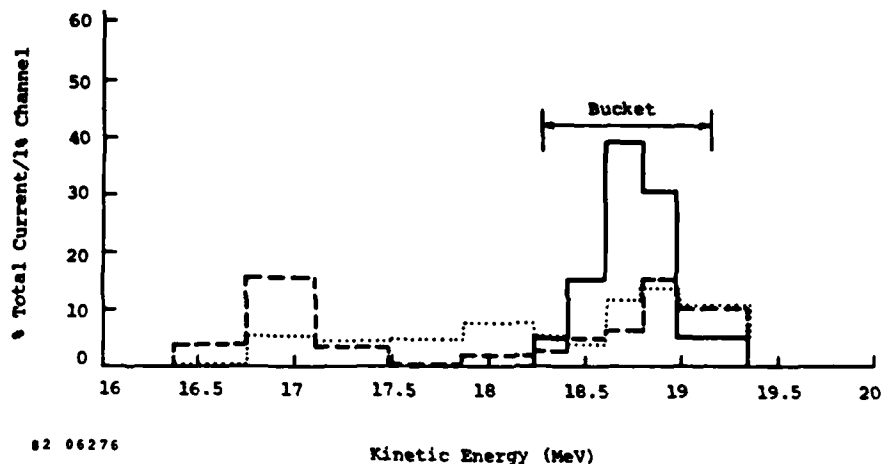


Figure 3-7. Electron Energy Spectra. The dotted and solid lines are measured spectra for a given macropulse, with and without photons, respectively. The dashed curve is a calculated output spectrum based on the solid line input spectrum, 400 MW CO_2 laser power, and ideal electron-photon overlap. The full width and location of the calculated ponderomotive potential well at the wiggler entrance is indicated.

nanoseconds prior to the laser pulse, and the dotted line shows the spectrum measured at the time of peak CO_2 intensity. The curves can be considered as input and output spectra, respectively, since the macropulse current and spectral content do not change significantly over a several nanosecond timescale. The photon pulse had a peak power of approximately 400 MW. In this case the spectrograph channels are shunted externally to an effective width of 1 percent from 18.2 to 19.0 MeV and a 2 percent effective width elsewhere. For any channel, the uncertainty in current at the time of maximum photon flux is not more than 25 percent. Another indication of the degree of reliability is that the total current, in the interaction and non-interaction traces, typically differs by less than 10 percent. The total current for each trace of Figure 3-7 is about 50 mA (macropulse current).

The shift of energy centroid from the input to the output spectra is 2.6 percent, assuming the current to be evenly distributed within each spectrograph channel. This 2.6 percent net extraction is the highest achieved to date in this experiment, but it is lower than initially expected. Using the input spectra of Figure 3-7, an electron energy spectrum including the interaction can be calculated using the initial (solid line) spectra by direct integration of the equations of motion⁽¹⁰⁾ for energy loss and electron phase in the ponderomotive potential. In this calculation, it is assumed that the e-beam is much smaller than the photon beam and is located precisely on the photon beam axis. The result is the dashed line curve of Figure 3-7, which yields a net extraction of 4.1 percent. The difference in peak deceleration for the two spectra is small, and could be the result of an energy offset between the actual and assumed entrance resonant energy. The curves differ most significantly at the intermediate energies around 18 MeV, where substantial current is found in the measurement, but not the calculation. This is the result of electron detrapping from the ponderomotive potential well in the central portion of the wiggler. Observation of the e-beam fluorescent spots within the wiggler shows that at most locations the e-beam is comparable in size to the $1/e$ radius of the photon electric field, but a quantitative measurement was not made due to the screen problems referred to in Section 3.1. If the e-beam is oversize, degradation of electron extraction then occurs due to both the effective loss of E-field and also to an apparent increase in electron energy spread caused by the B-field gradient. Both problems are expected to be unimportant in this experiment when the e-beam is within the $1/e$ envelope of the E-field. Some insight to the overlap problem should be possible if the e-beam can be filtered to a smaller size. Experiments to this end are in progress.

A parameterization of the extraction data with energy taken during report period is presented in Figure 3-8. The data show qualitatively correct energy resonance width, but the peak extraction values at 40 to 50 percent below prediction.

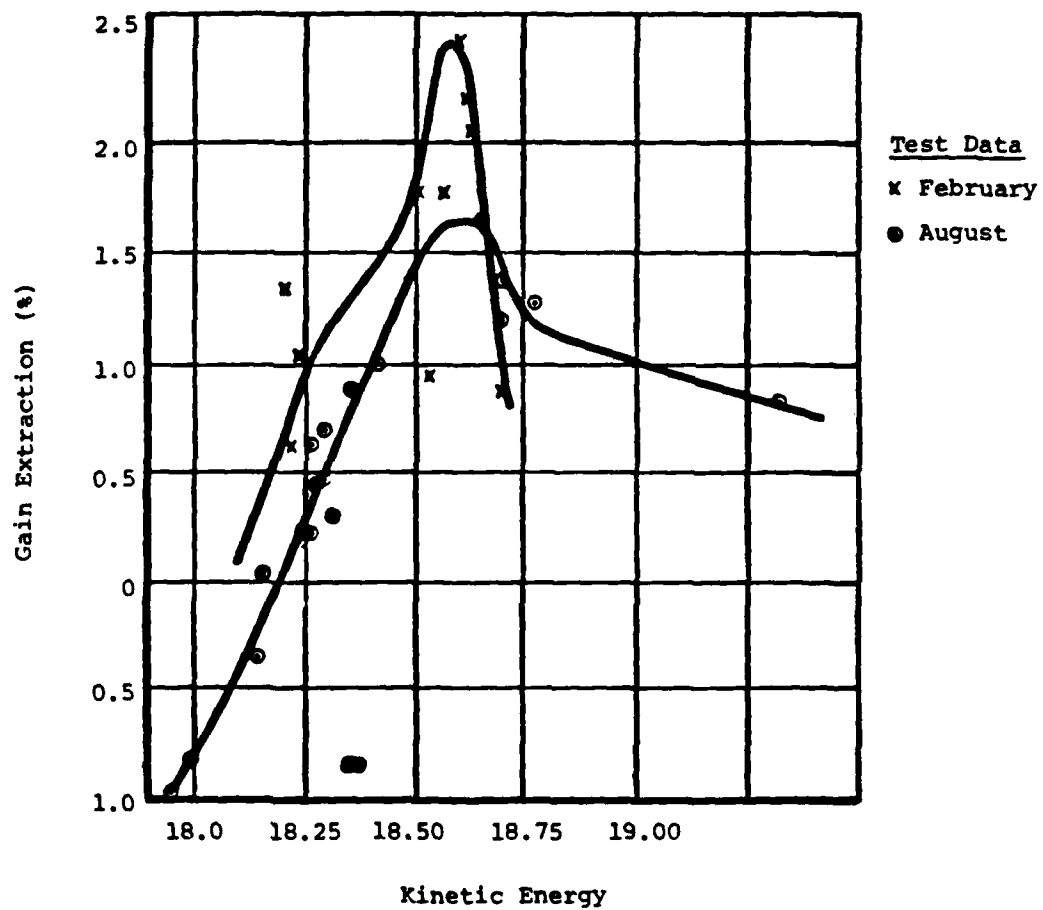


Figure 3-8. Extraction vs. Electron Beam Kinetic Energy.

Section 4

SUBHARMONIC PREBUNCHING INJECTOR

The subharmonic prebunching (SHPB) injector developed for the Phase I FEL experiments consists of the ARCO/RPC Model 12 electron gun, two standing wave single cavity bunchers (the first operating at one-sixth the fundamental frequency, and the second operating at the fundamental), a high gradient tapered phase velocity buncher, and finally a high gradient constant phase velocity buncher/accelerator. The injector is shown schematically in Figure 4-1.

4.1 SHPB INJECTOR DESIGN

The gun and injection system has been used to produce electron beams of ≈ 5 amperes peak micropulse current, with normalized emittance of $\epsilon = \pi \gamma x x' \leq 0.02$ cm-rad, and energy width of < 2 percent FWHM measured at FEL experiment. These parameters are for a steady state beam without subharmonic bunching. Transient operation of the injector/accelerator has shown 50A micropulse currents, again without the subharmonic buncher. Operation at high peak currents was initially limited by an inadequate axial magnetic field in the drift region of the fundamental frequency prebuncher. Our analysis showed that the addition of two large Helmholtz coils over the buncher and drift region were needed to reach the original design goal of 200A micropulse currents.

The analysis of the buncher injector section was performed to determine optimum settings for lenses and Helmholtz coils, buncher power and phase, and buncher drift distance. A variety of gun and buncher combinations were analyzed.

The radial extent of the electron beam from the gun through the injector lenses, solenoids, and bunchers is approximately calculated in the non-realistic paraxial equation.

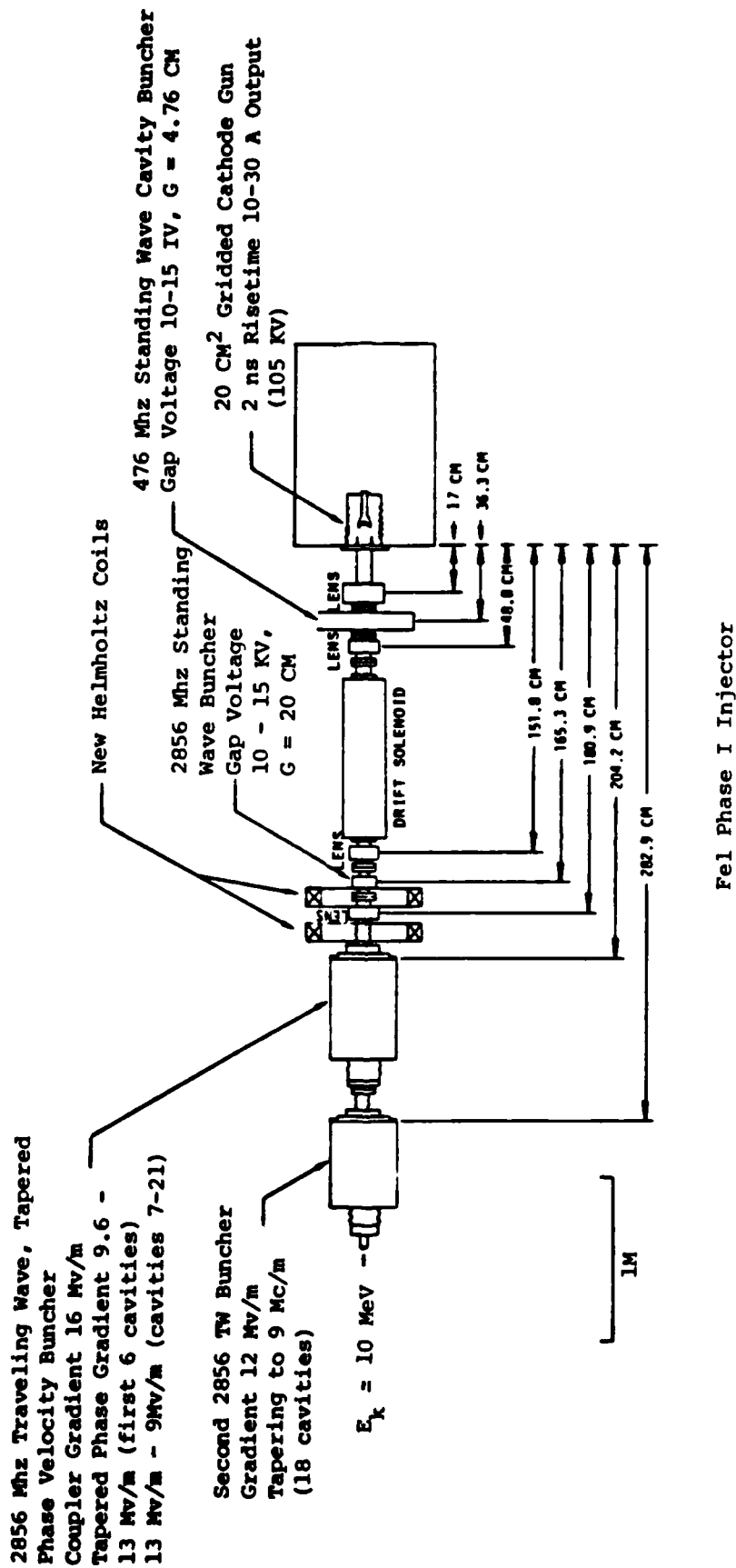


Figure 4-1. Schematic Drawing of FEL Phase I Injector.

$$\frac{d^2 r}{dz^2} + \frac{\eta^2 B_z^2}{8V} r - \frac{I(z)}{4\pi \epsilon_0 2NV^{-3/2}} \frac{1}{r} = 0$$

where (in SI units)

r = beam radius

η = e/m = electron charge/mass

V = electron energy in volts

I = beam current in amperes

B_z = axial magnetic field in

ϵ_0 = permittivity of free space

This equation has the form of a non-linear oscillator with forcing functions proportional to r and r^{-1} . In principle, radial control is achieved by

$$\frac{d^2 r}{dz^2} = 0$$

when B_z and I are constant, the constant value of the radius is just that for Brillouin flow. An important feature of this equation is the prediction of magnetic field variations for given radius, current, and initial beam parameters.

The paraxial treatment has been developed in a Boeing code which includes beam current ramping by the bunchers. The code also adjusts injector Helmholtz coils to fit a Brillouin flow magnetic field profile.

Two examples are given of the code calculation. The first, Figure 4-2 shows the effect of adding two additional Helmholtz coils to the fundamental buncher drift region. Without the coils there is no confinement for beams in excess of 20 amperes (5 ampere gun pulse times a factor of four current enhancement for the subharmonic buncher). Since the tapered phase buncher increases peak current by a factor of 3 to 4, this calculation predicts peak currents would be limited to less than 60

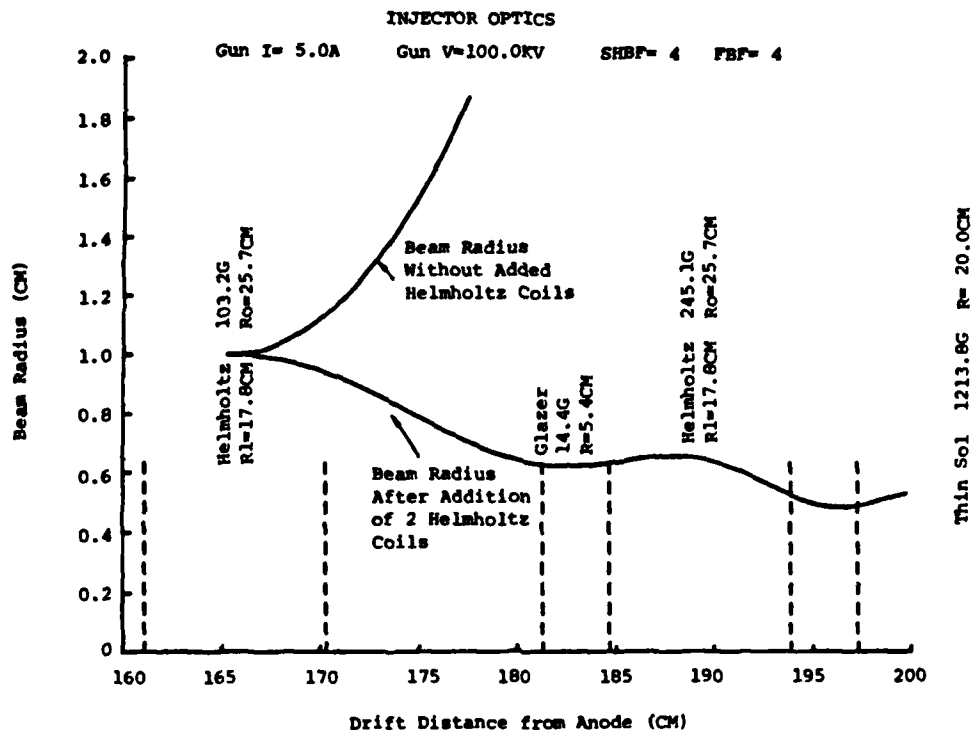


Figure 4-2. Paraxial Ray Calculation of Beam Size from Fundamental Buncher to Accelerator.

to 80 amperes without the added coils. This is not inconsistent with our measurement of 50A peak. The lower trajectory (with the coils) is for 5 amperes of gun current, amplified by four in the subharmonic and four in the fundamental buncher, for a peak current of 80A at the entrance to the tapered phase buncher. Additional charge phase compression due to the tapered phase buncher produces a final accelerated bunch current between 200A and 300A.

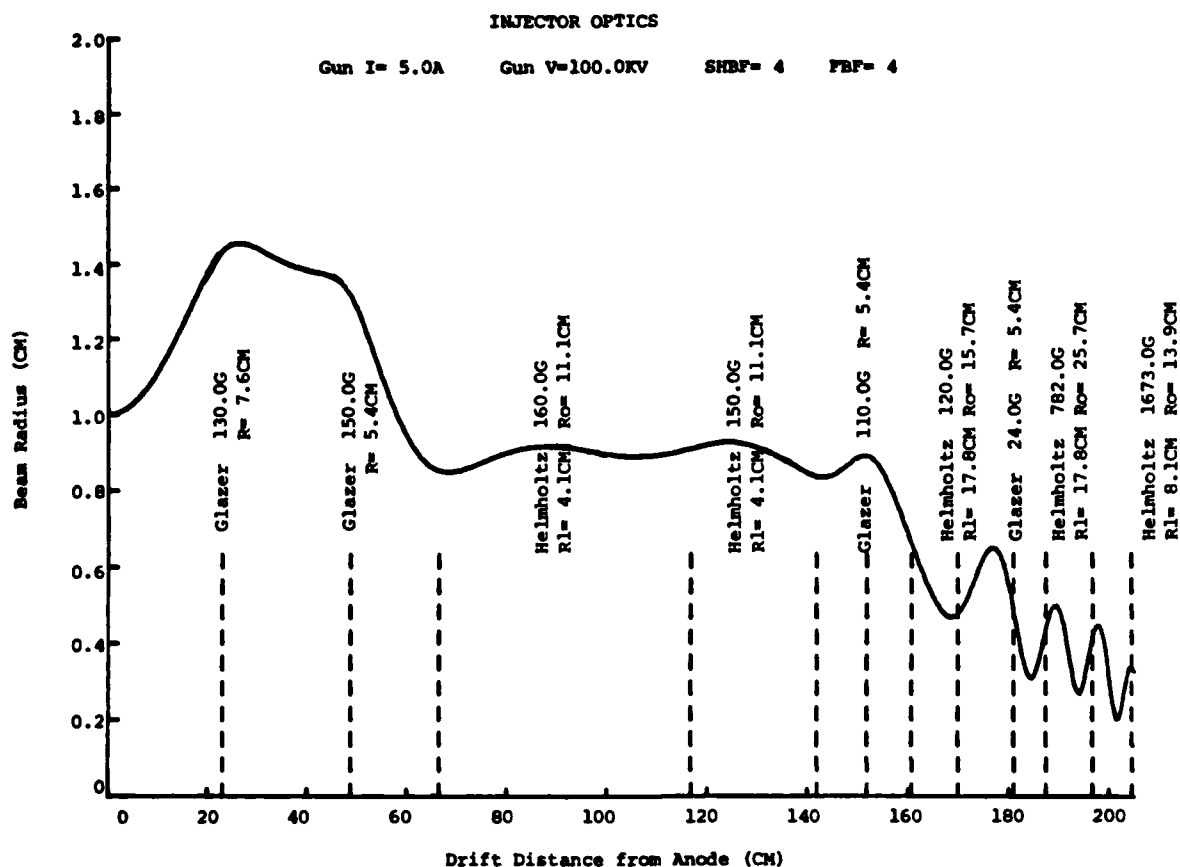


Figure 4-3. Paraxial Ray Calculation of Beam Size from Gun Anode to Accelerator.

Figure 4-3 is a trajectory plot for the entire injection beamline from the gun to the tapered phase buncher. The noticeable oscillations in the radial profile can probably be tuned out in practice by careful adjustment of the input lenses. Measurement of radial scalloping with diamagnetic loops in the injector may prove necessary to minimize emittance growth.

The interaction of the gated gun pulses and the standing wave cavity bunchers were analyzed using the code ORBIT developed by W.J. Gallagher. The beam model used is that described by Tein.⁽¹¹⁾ The derivation of the

equation of motion appropriate to prebunching is given in Reference 12. The approach is to consider the beam as a series of charged disks, ascribing all the beam charge to N disks per wavelength. The potential inside cylinder may be obtained, which conveniently eliminates infinities which would otherwise occur as disks approach each other infinitesimally close. The force on any disk may then be determined by summing over all other disks, and its motion calculated. This model, which permits crossovers, is considered realistic, since the disks are, in fact, "porous" from the electronic standpoint.

An ORBIT calculation, performed by Boeing, for the 476 MHz subharmonic prebuncher is shown in Figure 4-4. The calculation is for 5 nanocoulombs of charge in a 34-cm pulse length (one complete cycle time for the subharmonic frequency). The gun voltage was 100 kV and the modulation index α = gap voltage, V /gun voltage V_0 was 0.1. The

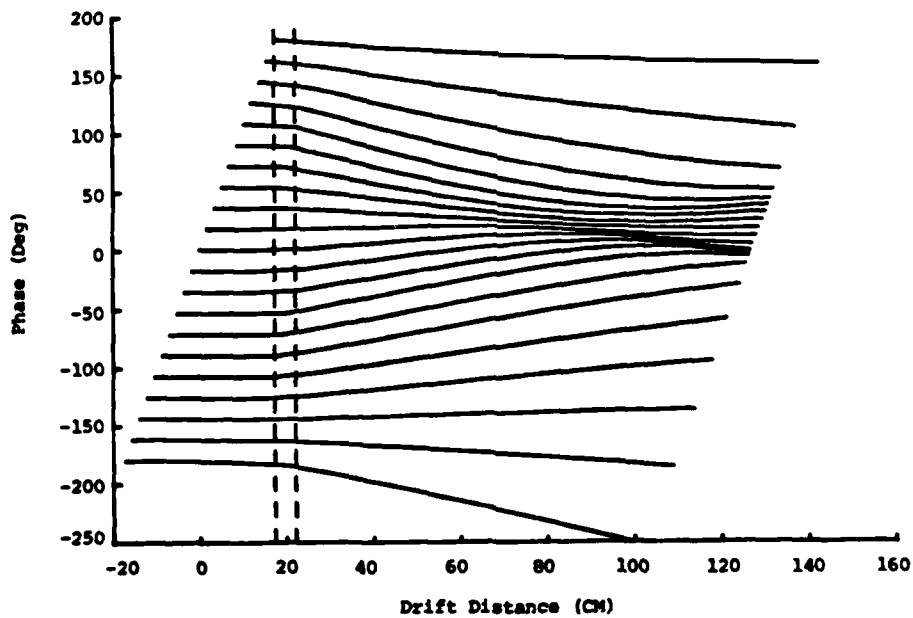


Figure 4-4. Subharmonic Buncher Phase Plot.

calculation shows 40 to 50 percentage of the charge bunches to roughly one radian of the subharmonic frequency. The resultant peak current at the crossover is ~8A. Additional bunching, in the fundamental prebuncher and traveling wave buncher, will result in 80 to 100A micropulse current.

The final elements in the injection system are a tapered phase velocity traveling wave buncher and a short constant phase velocity buncher section. These sections are operated at high gradient (roughly 14 MeV/meter) and utilize the "off crest" field gradient to offset the field difference across the bunch due to space charge. These sections were designed by J. Haimson and built by Varian Radiation Division with the design goal of very high beam current operation. Haimson's design calculation of phase orbits in the coupler and first four cavities of the tapered phase section is shown in Figure 4-5. The input current was 12

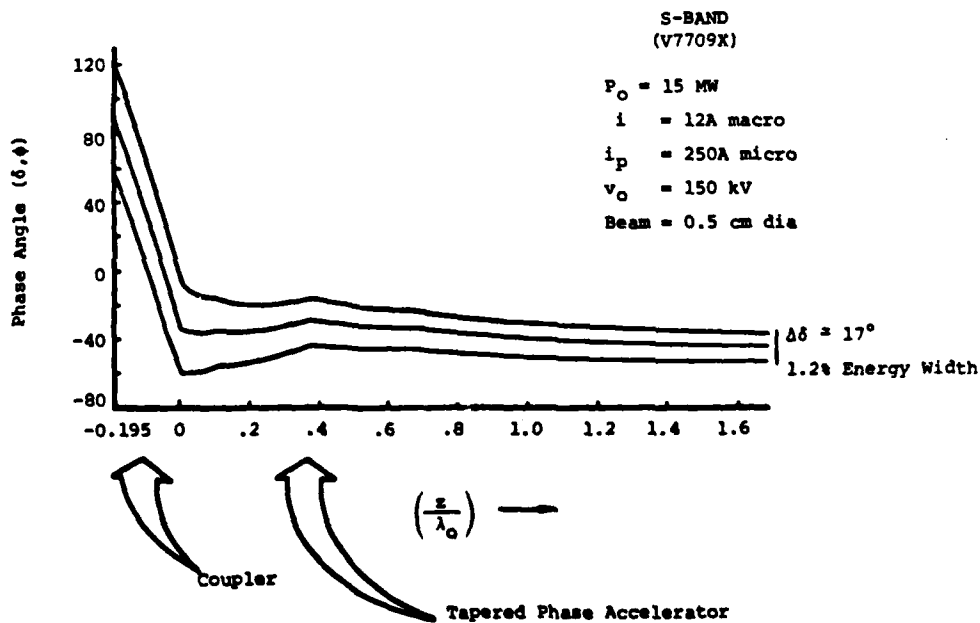
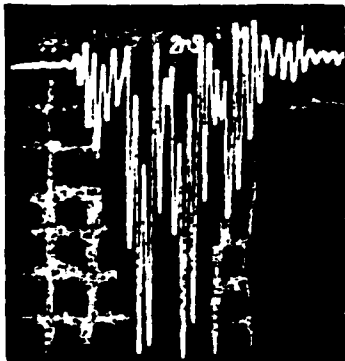


Figure 4-5. Bunching in Tapered Phase Accelerator Section (Space Charge Effects Included).

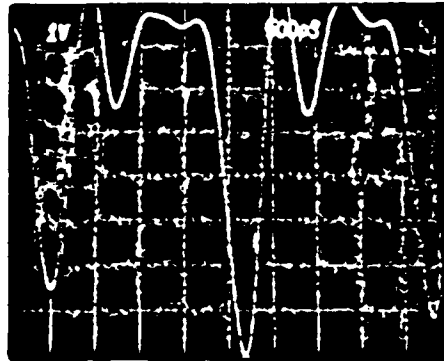
ampere macro (250A micropulse current). The final phase bunch is compressed to $\approx 17^\circ$ in phase, equivalent to 1.2 percent in energy width.

4.2 SEPB INJECTOR PERFORMANCE MEASUREMENTS

The subharmonic pulse current is shown in Figure 4-6. The first photograph shows the microstructure of the electron pulse. Modulation at the fundamental frequency (350 ps period), and the sixth harmonic (2.1 ns period), are clearly visible. The second photograph is a charge measurement from a 50 Ω Paraday cup (at approximately 1 GHz bandwidth). The major peaks shown are a composite of two fundamental micropulses. Somewhat more than half of the measured four nanocoulombs is found in the largest of the fundamental micropulses. Since the micropulse width consistent with the measured energy spread is 15 to 20 ps, the 2 to 2.5 nanocoulombs translates into a peak current of 100 to 150 amperes.



Pulse Structure with 2GHz Filter to Show
Relative Height of Satellites



Charge Measurement 8A PK x .5ns = 4 ncoul
1/2 - 2/3 goes into single bunch at 15-20 ps
I = 150A PK

Figure 4-6. Subharmonic Pulse Current.

The beam emittance was measured for short, high current pulses, both fundamentally and subharmonically bunched. These data are presented in Figures 4-7 and 4-8. The beam is profiled at two wire scanner stations separated by a 2.3 meter drift. A quadrupole doublet upstream of the first scan is used to form an approximate waist at the second scan station. The beam emittance, $\epsilon = \pi r \theta$, can be bounded by taking the downstream radius, r , and a convergence angle, θ , from the outside of the upstream beam to the outside of the downstream profile (as a minimum) for the axis at the downstream location (as a maximum), using this estimate for the fundamentally bunched beam

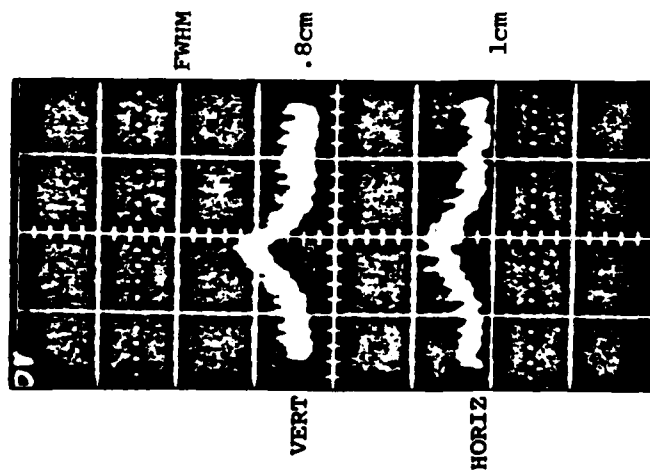
$$27 \text{ mm-mr} < \epsilon < 47 \text{ mm-mr}$$

and for the subharmonically bunched beam

$$27 \text{ mm-mr} < \epsilon < 57 \text{ mm-mr}.$$

The data were obtained at 20 MeV. In energy normalized units, the SHPB emittance range is 0.03 to 0.06 cm rad. In this data, the large number of subharmonic micropulses appeared to broaden the spatial profiles considerably. The subharmonic pulse energy spread measurement was made after the gun gate pulse was shortened to ~ 3 ns (FWHM). The measurement, shown in Figure 4-9, is for a subharmonic macropulse containing perhaps only two major micropulses. The energy measurement was obtained by imaging the beam at the energy slit location in the FEL beamline. A 3 mm input slit to the bend magnet was used. The measurement resolution was 0.5 percent. The subharmonic pulse spectral width was 1 to 1.5 percent.

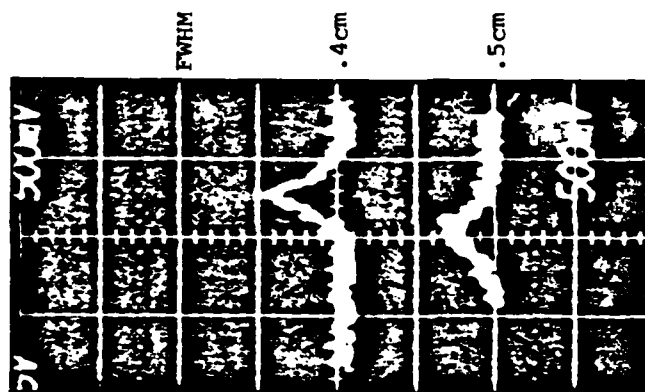
Upstream



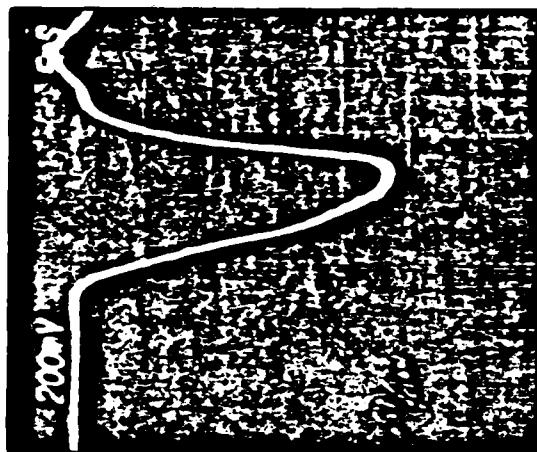
$$\epsilon = \pi r \theta$$

(MAX) 2π mm mr
(MIN) 4π mm mr

2.3M Downstream



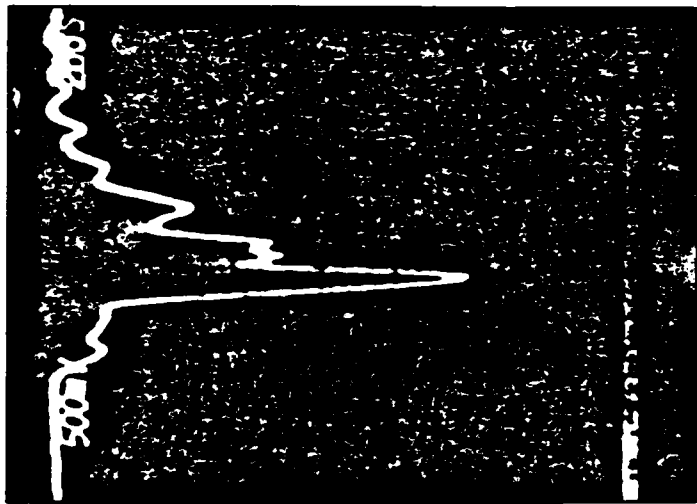
1 cm/div



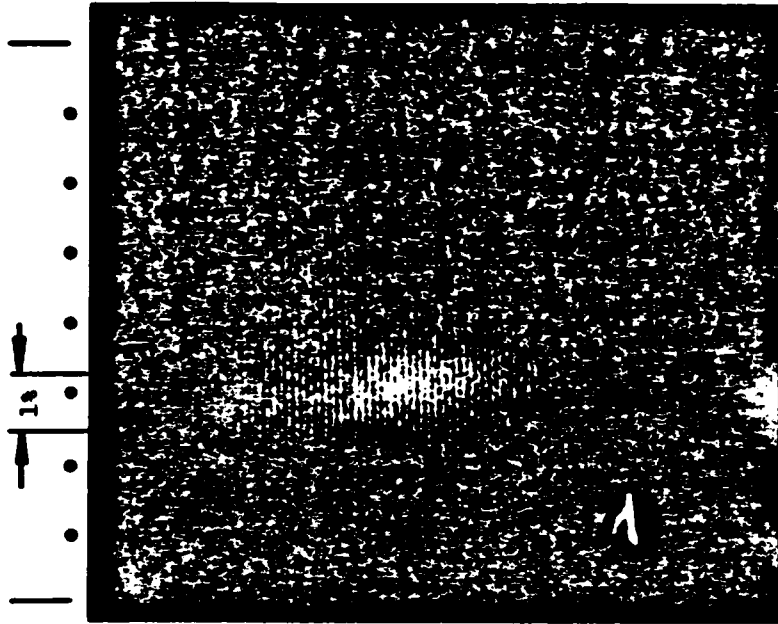
3.5 A Macro
~8 ns FWHM
 $I_\mu > 50A$

Figure 4-7. Short Macropulse Emittance.





~3 A (Macro)
2 nd/div



Intensifier at Energy Slit Location (Slits Out)
Input Slit 3 mm
Resolution ~.5%

Figure 4-9. Subharmonic Pulse Energy Spread.

Section 5

SUMMARY

During this reporting period a single-pass extraction experiment using a tapered wiggler has been constructed and put into operation. The experiment has provided a demonstration of the large single-pass kinetic energy extraction possible with the tapered wiggler. Major system elements constructed are: 1) 2.2 meter SmCo₅ wiggler with a 9 percent energy taper, 2) gigawatt class CO₂ laser operating on a single longitudinal and transverse mode, 3) electron transport system, beam position and profile diagnostics, and electron spectrograph. The extraction spectra obtained are consistent with the tapered wiggler theory so long as an imperfect electron-photon overlap is taken into account. Specifically, a deceleration of 9 percent has been observed in accordance with theory. In addition, 2.5 percent net extraction has also been achieved; this to be compared to a design value of 4 percent for the case of perfect overlap. While the cause of the non-ideal overlap has not been specifically demonstrated, i.e., not quantitatively apportioned between steering errors, focusing errors, and excess emittance, it is expected that improved overlap can be achieved in upcoming tests by further reduction of the emittance and thereby achieve the desired 4 percent extraction result.

The subharmonic buncher has been installed and successfully operated on the Boeing Linac. This work is directed toward obtaining high current, low emittance, and low energy spread micropulses necessary for future tapered-wiggler oscillator experiments. The data presented in this report show peak currents of 100 to 150 amps and an emittance of 27 - 57 mm-mr at 20 MeV, with an energy spread of less than 2 percent.

REFERENCES

1. D.A.G. Deacon, L.R. Elias, J.M.J. Madey, G.J. Ramian, H.S. Schwettman, and T.I. Smith, "First Operation of a Free-Electron Laser," Phys. Rev. Lett. 38, 892 (1977).
2. K.L. Brown, "TRANSPORT, A Computer Program for Designing Charged Particle Beam Transport Systems", SLAC-75, Rev. 3 (August 1972).
3. D.A. Swenson, "Achromatic Translation System for Charged Particle Beams," Rev. Sci. Instr. 35, 608 (1964).
4. D.C. Carey, "TURTLE, A Computer Code for Simulating Charged Particle Beam Transport Systems," NAL-64 (May 1978).
5. K. Halbach, "Physical and Optical Properties of Rare Earth Cobalt Magnets." Presented at International Conference on Charged-Particle Optics, Giesses, West Germany, September 1980.
6. J.M. Slater, "Tapered-Wiggler Free-Electron Laser Optimization," IEEE J. Quant. Elect. QE-17, 147 (1981).
7. A.J. Campillo, J.E. Pearson, S.L. Shapiro, and N.J. Terrell, "Fresnel Diffraction Effects in the Design of High Power Laser Systems" Appl. Phys. Lett. 23, 85 (1973)
8. J. Lobb, L'onde Electrique 27, 27 (1947).
9. D.C. Quimby, "Floating Wire Measurement of Transverse Magnetic Field Errors in a Planar Free-Electron Laser Wiggler", J. Appl. Phys. 53, 6613 (1982).

10. J.M.J. Madey, D.A.G. Deacon, L.R. Elias, and T.I. Smith, "An Approximate Technique for the Integration on the Equations of Motion in a Free-Electron Laser", *Il Nuovo Cimento* 51, 53 (1979).
11. P.K. Tein, et.al., *Proc IRE* 43, 20 (1955).
12. M. MacGregor and C.B. Williams, *IEEE Trans. Nucl. Sci.* NS-14, 581 (1967), and G.W. Peterson and W.J. Gallagher, *IEEE Trans. Nucl. Sci.* NS-16, 214 (1967).

REFERENCES

1. D.A.G. Deacon, L.R. Elias, J.M.J. Madey, G.J. Ramian, H.S. Schwettman, and T.I. Smith, "First Operation of a Free-Electron Laser," Phys. Rev. Lett. 38, 892 (1977).
2. K.L. Brown, "TRANSPORT, A Computer Program for Designing Charged Particle Beam Transport Systems", SLAC-75, Rev. 3 (August 1972).
3. D.A. Swenson, "Achromatic Translation System for Charged Particle Beams," Rev. Sci. Instr. 35, 608 (1964).
4. D.C. Carey, "TURNING, A Computer Code for Simulating Charged Particle Beam Transport Systems," NAL-64 (May 1978).
5. K. Halbach, "Physical and Optical Properties of Rare Earth Cobalt Magnets." Presented at International Conference on Charged-Particle Optics, Giessen, West Germany, September 1980.
6. J.M. Slater, "Tapered-Wiggler Free-Electron Laser Optimization," IEEE J. Quant. Elect. QE-17, 147 (1981).
7. A.J. Campillo, J.E. Pearson, S.L. Shapiro, and N.J. Terrell, "Fresnel Diffraction Effects in the Design of High Power Laser Systems" Appl. Phys. Lett. 23, 85 (1973)
8. J. Lobb, L'onde Electrique 27, 27 (1947).
9. D.C. Quinby, "Floating Wire Measurement of Transverse Magnetic Field Errors in a Planar Free-Electron Laser Wiggler", J. Appl. Phys. 53, 6613 (1982).

10. J.M.J. Madey, D.A.G. Deacon, L.R. Elias, and T.I. Smith, "An Approximate Technique for the Integration on the Equations of Motion in a Free-Electron Laser", *Il Nuovo Cimento* 51, 53 (1979).
11. P.K. Tein, et.al., *Proc IRE* 43, 20 (1955).
12. M. MacGregor and C.B. Williams, *IEEE Trans. Nucl. Sci.* NS-14, 581 (1967), and G.W. Peterson and W.J. Gallagher, *IEEE Trans. Nucl. Sci.* NS-16, 214 (1967).

1. "An
Lons of Motion
9).

NS-14, 581

END

DATE
FILMED

7-8

DTIC